# Infrared microscopic imaging of cutaneous wound healing: lipid conformation in the migrating epithelial tongue

Guo Yu
Olivera Stojadinovic
Marjana Tomic-Canic
Carol R. Flach
Richard Mendelsohn

# Infrared microscopic imaging of cutaneous wound healing: lipid conformation in the migrating epithelial tongue

**Guo Yu,[a] Olivera Stojadinovic,[b] Marjana Tomic-Canic,[b] Carol R. Flach,[a] and Richard Mendelsohn[a]**
[a]Rutgers University, Newark College of Arts and Science, Department of Chemistry, 73 Warren Street, Newark, New Jersey 07102
[b]University of Miami Miller Medical School, Department of Dermatology & Cutaneous Surgery, Wound Healing and Regenerative Medicine Research Program, 1600 NW 10th Avenue, RMSB 2nd Floor, Miami, Florida 33136

**Abstract.** Infrared microscopic imaging has been utilized to analyze for the first time the spatial distribution of lipid structure in an *ex vivo* human organ culture skin wound healing model. Infrared images were collected at zero, two, four, and six days following wounding. Analysis of lipid infrared spectral properties revealed the presence of a lipid class with disordered chains within and in the vicinity of the migrating epithelial tongue. The presence of lipid ester $C = O$ bands colocalized with the disordered chains provided evidence for the presence of carbonyl-containing lipid species. Gene array data complemented the biophysical studies and provided a biological rationale for the generation of the disordered chain species. This is the first clear observation, to our knowledge, of disordered lipid involvement in cutaneous wound healing. Several possibilities are discussed for the biological relevance of these observations. © *2012 Society of Photo-Optical Instrumentation Engineers (SPIE).* [DOI: 10.1117/1.JBO.17.9.096009]

## 1 Introduction

The healing of cutaneous wounds is a highly temporally and spatially coordinated process occurring in three sequential, yet overlapping stages. Initial rapid sealing of the damaged site is achieved via clot formation. Re-epithelization commences within a few hours of the injury and requires activation, proliferation, and migration of keratinocytes from the wound edge to cover the denuded wound area. The keratinocyte layer (known as the migrating epithelial tongue) covers the wound bed within seven to nine days. This process is followed by the reformation of a stratified epidermal layer and finally matrix remodeling that may last up to a year.[1]

The molecular components and control mechanisms involved at various stages of the healing process have been analyzed extensively. Molecular techniques have monitored the spatial distribution of particular keratins as healing progresses.[2–4] In contrast, biophysical approaches for imaging the spatial distribution and structural characteristics of particular molecules such as lipids, proteins, or exogenous materials in the healing tissue are sparse. Such information is of particular interest for characterization of therapeutic interventions, including the study of interfaces between native skin and three-dimensional skin equivalents, and the action and spatial distribution of exogenous agents.

The paucity of biophysical imaging studies of wound healing arises from the lack of available technologies to carry out such experiments. The standard high-resolution structural methods of biophysics [x-ray diffraction, nuclear magnetic resonance (NMR)] are inapplicable in heterogeneous tissue environments. Thus, different methods that can identify and image tissue constituents and molecular structure are required. In the past 15 to 20 years, Fourier transform infrared (FTIR) microscopic imaging has evolved to study tissues[5,6] and to characterize pathological states.[7] The approach provides spatially resolved compositional and molecular structure information. The experiment produces a full IR spectrum from each pixel and requires neither probe molecules nor application of stains. A single IR imaging dataset generates a multitude of images, each displaying the spatial distribution of an IR spectral parameter. IR measurements are generally performed in the transmission mode and require microtoming of sections to a thickness of $\sim 5$ $\mu$m. IR absorption provides intense signals (molar extinction coefficients range up to $10^3$); thus, high-quality spectra may be generated fairly quickly (6,000 to 10,000 complete mid-IR spectra from pixels of dimension $\sim 6 \times 6$ $\mu$m may be acquired in 40 min), and images from millimeter-sized areas may be readily generated.

We have recently used both IR microscopic imaging and confocal Raman microscopy to monitor the permeation and metabolism of exogenous agents in skin and to track natural moisturizing factor levels and solvent-induced structural changes in single corneocytes.[8,9] In addition, in our first wound healing study,[2] we used an *ex vivo* cutaneous wound-healing model in combination with immunohistochemistry and gene array analysis to correlate the gene expression profile with IR images during re-epithelization. Multivariate statistical analyses of IR images were correlated with immunofluorescence staining patterns, demonstrating the feasibility of acquiring structural and spatial information from the major proteins involved in wound healing.

In the current study, we focused on the evaluation of lipid structure in the vicinity of the migrating epithelial tongue (MET). Aside from proteins, the major contributor to the IR

Address all correspondence to: Carol R. Flach, Rutgers University, Newark College of Arts and Science, Department of Chemistry, 73 Warren Street, Newark, NJ 07102. Tel: +973-353-1330; Fax: 973-353-1264; E-mail: flach@andromeda.rutgers.edu

spectra of skin arises from lipid components. In addition, the study of skin lipids by IR spectroscopy and imaging has been widespread over the past decade.[10–13] Robust correlations between vibrational spectra and lipid chain conformational order and packing have thereby become available.[14] Therefore, we used IR microscopic imaging to evaluate the lipid chain conformation within and in the vicinity of the MET at various time points following wounding. A thorough perusal of the wound healing literature has produced only two experimental results evaluating changes in skin lipids during wound healing. A bioanalytical report from Kozel'tsev et al.[15] tracked lipid content in a rat skin wound field. A four-fold increase in triglyceride levels was observed five days into regeneration, especially in the granulation tissue. In addition, Vicanova et al.[16] used skin substitutes grafted onto athymic nude mice as a long-term model for the stratum corneum (SC) barrier organization. The initially impaired barrier was restored to near normal at six months postgrafting. In additional studies by several groups over the past decade,[17–20] the putative role of lipid rafts in controlling the function of cell signaling molecules, involving the epidermal growth factor receptor (EGFR), has been investigated through biochemical and molecular approaches. EGFR controls keratinocyte proliferation and motility. Here, we utilized IR imaging and gene array analysis to further elucidate the spatial distribution and conformational order of lipids during *ex vivo* wound healing.

## 2 Materials and Methods

### 2.1 *Human Organ Culture Wound Healing Model*

Human skin specimens were obtained from reduction surgery in accordance with institutional protocols and used to generate acute wounds as previously described.[21] A 3-mm biopsy punch was used to create an acute wound and skin specimens were maintained at the air-liquid interface with Dulbecco's modified Eagle's medium (DMEM) (BioWhittaker), antibiotic/antimycotic and fetal bovine serum (Gemini Bio-Products) at 37°C, 5% $CO_2$, and 95% relative humidity. Specimens were collected for further analyses at zero, two, four, and six days postwounding.

### 2.2 *Gene Array Data Analysis*

Microarray Suite 5.0 (Affymetrix) was used for data extraction and for further analysis. Data mining tool 3.0 (Affymetrix, Santa Clara, CA) and GeneSpring software 7.3.1 (Silicon Genetics, Redwood City, CA) were used for normalization, degree of change, and *p*-value calculations. Samples were normalized per chip to the 50th percentile and per gene to a median. Statistical comparisons of expression level between each condition were performed using ANOVA test. Only genes with a *p*-value less than 0.05 were considered to be statistically significant. Differential expressions of transcripts were determined by calculating the degree of change. Genes were considered regulated if the expression levels differed more than two-fold relative to healthy, unwounded skin.

### 2.3 *IR Imaging Experiments*

For IR imaging, samples were flash frozen with liquid nitrogen and stabilized at $-30°C$ on a chuck within a Bright/Hacker 5030 Microtome (Bright Instrument Company, Huntington, UK/ Hacker Instruments, Fairfield, NJ) oriented so that sections (~5 $\mu$m thick) were cut perpendicular to the SC. Sections placed on $CaF_2$ IR windows were generally mapped across both unwounded and wounded areas using a Perkin-Elmer Spotlight system (Waltham, MA) equipped with an essentially linear array ($16 \times 1$ detector elements) mercury-cadmium-telluride detector. A high-precision XY sample stage permitted the collection of IR images (pixel area of 6.25 $\mu m^2$) over ~0.5 × 0.5 mm sample areas. Spectral resolution was 8 $cm^{-1}$. Overall, three sets of separate skin specimens were prepared and analyzed. Results shown are representative of all three sets.

### 2.4 *IR Data Analysis*

IR spectra were analyzed using ISYS software version 3.1 (Malvern Instruments, LTD, UK). Image planes of spectral parameters and factor analysis scores were generated after linear baselines were applied over spectral regions of interest. Factor analysis, as detailed elsewhere,[5] is a statistical multivariate technique that reduces the dimensionality of the data by detecting patterns in the relationships between observed variables. The approach begins with principal component analysis (PCA) followed by a score segregation routine that seeks transformations between the PCA loadings and Beer's Law parameters. Factor analysis results in a set of factor loadings and factor scores that depict the correlations between the actual spectrum at each pixel and the factor loadings. The calculated factor loadings resemble typical spectra, although not of pure components. Usually three to six significant factors are observed in a wound healing dataset.

## 3 Results

### 3.1 *IR Imaging Identifies Changes in Epidermal Lipid Composition During Wound Healing*

A typical sequence of events in the current skin wound healing explant model is depicted in a series of visible micrographs from separate sections at various times (control, zero, two, four, and six days) following wounding, as shown in Fig. 1. In the unwounded control skin, the SC is clearly evident at the top of the micrograph. The image acquired immediately following wounding (day zero) shows both the presence of the residual SC at the top right as well as the wounded area on the left lacking the more dense SC tissue. The MET becomes visible covering some ~3/4 to ~7/8 of the surface from the right-hand to the left-central areas of the day two and day four images, respectively. Coulombe[22] state that the MET arises from elongated keratinocytes that originate from the basal and suprabasal layers of the epidermis near the wound. In the current instance, the presence of the MET indicates that epithelization occurs in the explants and thus provides evidence for the validity of the model for biophysical studies. No uncovered area was found in the day six image, suggesting that the MET had covered the entire wounded area, i.e., the epithelization stage was complete.

The visible micrographs in Fig. 1 do not contain molecular-level information and thus cannot be used to identify molecular constituents present in the image. IR microscopic analysis permits identification of particular molecular classes, and furthermore, permits elucidation of structural characteristics of particular constituents. Typical, single-pixel, raw IR spectra from different skin regions are overlaid in Fig. 2 with bands of interest marked. The high signal-to-noise levels in the spectra are immediately apparent. Subtle changes in several bands are observed comparing the spectra of different skin regions.
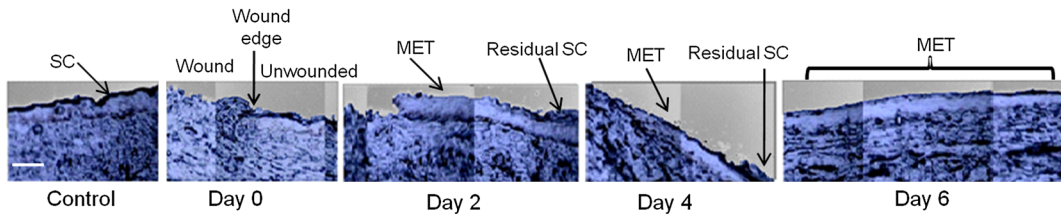
**Fig. 1** Visible images of microtomed wound healing sections. The control is a nonwounded section of human skin (left image) and the remaining images are marked according to a postwounding timeframe (left to right, day zero, two, four, and six). The 100-$\mu$m scale bar applies to all the images.
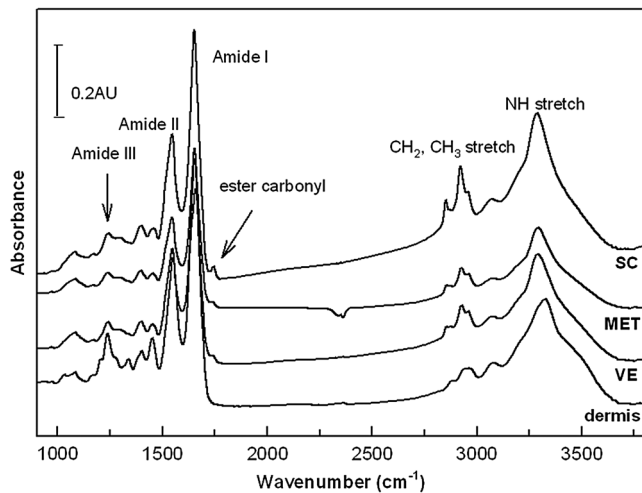


**Fig. 2** Typical single-pixel IR spectra from various regions of microtomed human skin sections: stratum corneum (SC), migrating epithelial tongue (MET), viable epidermis (VE), and dermis as marked. Spectra of the SC, VE, and dermis were obtained from the day zero section (see Fig. 1) in the unwounded area and the spectrum of the MET was acquired from the day two section.

Our analytical strategy was to apply factor analysis to the IR images within spectral regions known to be sensitive to particular aspects of molecular structure.

The sensitivity of several IR spectral regions to various aspects of skin, wound constituents, and particular elements of molecular structure are shown in Figs. 3 to 7. Figure 3(a) shows two factor loadings in the 1490 to 1720 cm$^{-1}$ region, which encompasses the Amide I (mostly peptide bond C = O stretch, frequency region 1620 to 1690 cm$^{-1}$) and Amide II (mostly mixed N-H in-plane bend and C = N stretch, frequency region 1510 to 1560 cm$^{-1}$) vibrational modes. The factor loadings predominantly arise from keratin-rich and collagen-rich regions of the tissue. The Amide I spectral region shows substantial differences between these two proteins and provides a powerful means to distinguish between them in skin tissue. Collagen is characterized by a major Amide I peak near 1660 cm$^{-1}$ and a shoulder near 1636 cm$^{-1}$ while keratin is characterized by a more symmetric single band at 1652 cm$^{-1}$. Significant differences in the Amide II patterns are also noted. Images of the factor scores for this spectral region in the day zero and day two samples help us to distinguish keratin in the epidermis and MET from the underlying dermis [Fig. 3(b), top and bottom, respectively]. The chemical identification of proteins known to be located at particular sites [see
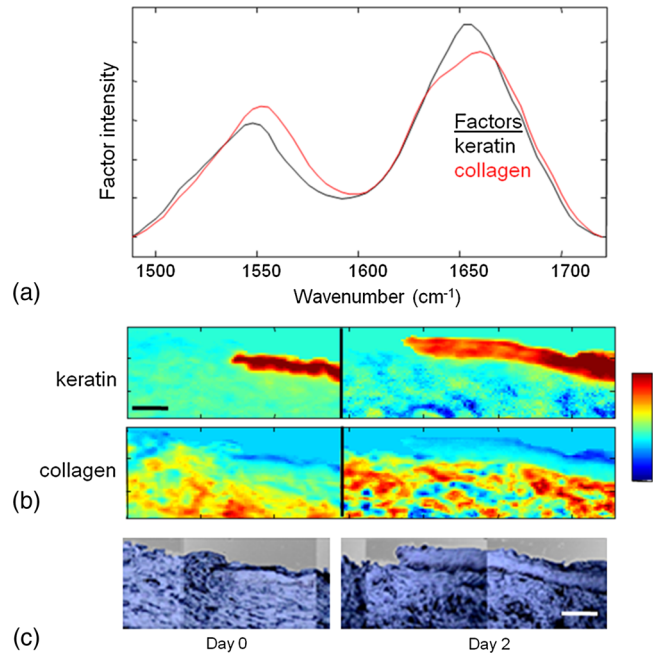


**Fig. 3** Detection and IR characterization of the spatial distribution of keratin-rich and collagen-rich regions in day zero and day two *ex vivo* wound healing model human skin sections utilizing factor analysis conducted over the 1490 to 1720 cm$^{-1}$ region. (a) Two factor loadings in the 1490 to 1720 cm$^{-1}$ region. (b) IR score images for two factor loadings with color coding scale bar of scores as follows: red > yellow > blue. (c) Visible images of the two sample sections. The 100-$\mu$m scale bar applies to all the images.

visible images in Fig. 3(c)], e.g., keratin in the MET, collagen in the dermis, provides a useful validation of the factor analysis method.

Factor loadings and score images from the C-H stretching region (2800 to 3000 cm$^{-1}$) calculated from the full set of skin sections (Fig. 1) are shown in Fig. 4(a) and 4(b), respectively. This spectral region was not analyzed in our prior study. The spectral patterns arise from relatively conformationally ordered (L1) or disordered (L2) lipid acyl chains. Acyl chains that are conformationally well-ordered, essentially all-trans, are characterized by methylene symmetric stretching ($\sim$2850 cm$^{-1}$) and asymmetric stretching ($\sim$2920 cm$^{-1}$) frequencies shifted down by 2 to 4 cm$^{-1}$ from their counterparts in disordered chains. In our study, the methylene symmetric stretching mode ($\nu_{sym}$ CH$_2$) is shifted from $\sim$2854.5 to 2852.7 cm$^{-1}$ while the asymmetric stretching mode shifted from 2925.4 to 2922.3 cm$^{-1}$, reflecting an increased degree of conformational order in the chains.
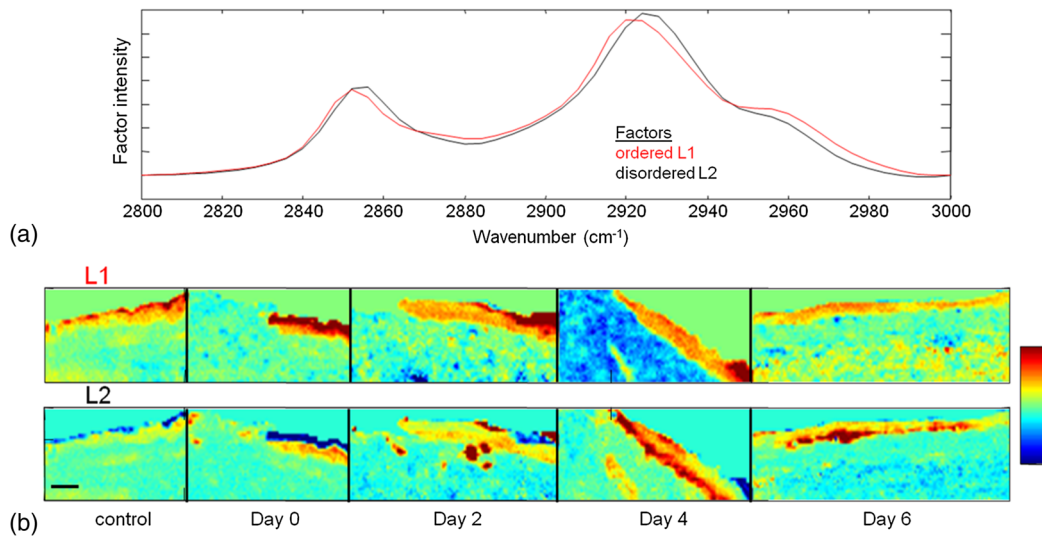
**Fig. 4** IR characterization of acyl chain conformational order (factor analysis conducted over the 2800 to 3000 cm$^{-1}$ region) of a nonwounded control and wounded skin sections at time points zero, two, four, and six days postwounding. (a) Factor loadings of L1, ordered chains (red) and L2, disordered chains (black). (b) Score images of L1 and L2 for the control and day zero, two, four, and six sections as marked. The 100-$\mu$m scale bar applies to all the images.
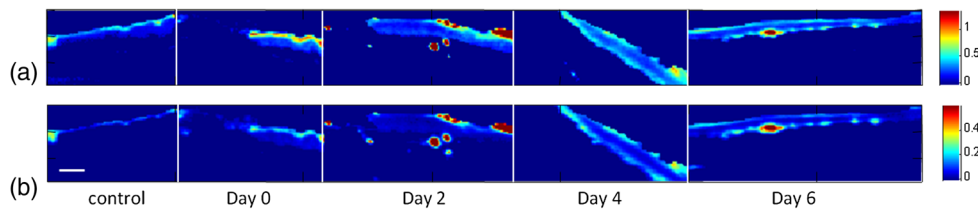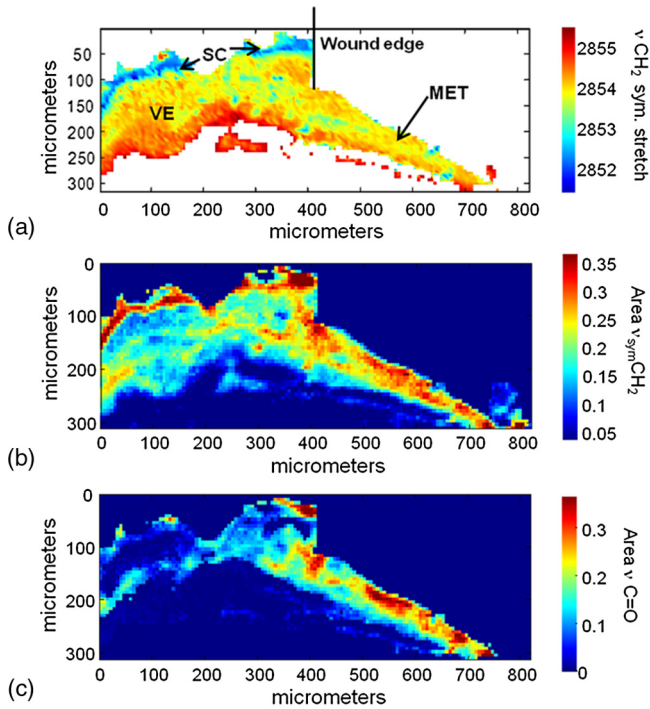


**Fig. 5** Images of univariate IR spectral parameters for the nonwounded control sample and wounded skin sections at time points zero, two, four, and six days postwounding. The integrated area of the symmetric CH$_2$ stretching band (2840 to 2868 cm$^{-1}$) is displayed in (a) and provides a semi-quantitative measure of the lipid acyl chain concentration. The integrated area of the high-frequency half of the lipid carbonyl (1744 to 1756 cm$^{-1}$) is displayed in (b). The high-frequency half of the band was used to avoid interference from the incompletely resolved strong Amide I band (see Fig. 2). The 100-$\mu$m scale bar applies to all the images.

Concatenated images of factor scores generated from the loadings (L1 and L2) in the methylene stretching region are shown in Fig. 4(b) from the control skin and day zero, two, four, and six wound sections. The highest scores from the ordered lipid factor labeled L1 in the control and the period immediately following wounding (day zero) coincide with the SC as observed in the visual micrographs. The factor score images for L1 also confirm the identification of a small region of residual SC on the right side of the day two and four wound sections. In addition, slightly lower scores for factor L1 were observed in the nonwounded area of the viable epidermis (VE) (control, day zero and two) and throughout the MET (day two to six). Upon wounding, the spatial and temporal evolution of scores for the disordered lipid factor, L2, is notable. Scores are quite low throughout the entire area of the control skin sample and appear somewhat higher in the VE at day zero. The dark blue area limited to the top ~10 to 20 $\mu$m in the control and at day zero and two in the images represents very low scores for the disordered lipid factor (L2) in the SC as anticipated. In the day two image, small pockets with high scores, mostly in the area basal to the MET, were observed, prior to spreading throughout the basal area and leading edge of the MET on day four. The day six section displays high scores concentrated in the lower to middle regions of the newly formed epidermal layer.

A simple univariate measure was used to analyze the spatial distribution of the relative concentration of lipid in the dataset. The images shown in Fig. 5(a) were generated from the integrated area of the $\nu_{sym}$ CH$_2$ stretching band. The regions with high lipid content coincide with the ordered lipid located in the SC, as described above for Fig. 4(b) (L1 images) and with the disordered lipid (L2 images), especially the lipid pockets in the day two and day six sections. To aid in the identification of the chemical species of the disordered lipid, factor analysis was performed on the lipid C = O (1720 to 1770 cm$^{-1}$) stretching region (results not shown). Two major factors were observed, differing by about 2 cm$^{-1}$ in carbonyl peak position. Both peak positions (1743 and 1745 cm$^{-1}$) are characteristic of (lipid) ester carbonyls, although the origin of the difference is unknown. To further probe the spatial distribution of the lipid carbonyl content, the integrated area of this band was measured and the data is displayed in Fig. 5(b) for the wound healing dataset. The areas with the highest concentration of lipid carbonyl intensity overlap with regions of high lipid acyl chain concentration [Fig. 5(b)] in the day two, four, and six sections and notably with the disordered lipid pockets as mentioned above.

**Fig. 6** Images of univariate IR spectral parameters for a day six post-wounding section delineating (a) lipid acyl chain conformational order via the methylene symmetric stretching frequency, (b) relative lipid acyl chain concentration via the integrated area of the methylene symmetric stretching band (2840 to 2864 cm$^{-1}$), and (c) relative lipid ester concentration via the integrated area of the C $=$ O stretching band (1728 to 1772 cm$^{-1}$).

An alternative means to characterize the physical state of the lipid present in a healing wound from a similar skin specimen six days after wounding is presented in Fig. 6. We used a different manner of univariate measure to directly image lipid conformation via the methylene symmetric stretching frequency [Fig. 6(a)]. Herein, the 1 to 2 cm$^{-1}$ increase due to chain disorder in $v_{sym}$ CH$_2$ comparing the SC to the VE is directly evident [Fig. 6(a)]. This type of univariate measure represents an average of the proportions of ordered and disordered lipid at a given location, whereas factor analysis provides separate images of ordered and disordered lipid species. In Fig. 6(a), lipids with disordered acyl chains, average $v_{sym}$ CH$_2$ observed at 2854 to 2854.5 cm$^{-1}$, are observed throughout the MET and VE in the nonwounded area, along with the more ordered lipids of the SC ($v_{sym}$ CH$_2$ at ~2852 cm$^{-1}$).

A measure of the integrated area of the methylene symmetric stretching band, an approximate monitor of relative lipid acyl chain concentration, is displayed in Fig. 6(b). An equivalent plot for the lipid C $=$ O stretch is shown in Fig. 6(c). Comparison of Fig. 6(b) and 6(c) reveals that there is quite an overlap of area in the MET with both high methylene and carbonyl stretching intensities. Small pockets at the edge of the wound are observed as well. However, the integrated area of both stretching modes appears to be lower in the bulk of the nonwounded VE. As anticipated, high methylene intensity in the SC [Fig. 6(b)] is also evident in the image.

Further characterization of lipid, collagen, and keratin molecules is available through factor analysis of the 980 to 1480 cm$^{-1}$ region (Fig. 7). We used the same wound specimens as shown in Fig. 1. The three factor loadings shown in Fig. 7(a) reveal distinct spectral features unique to different chemical species as deduced from their spatial distributions displayed in the
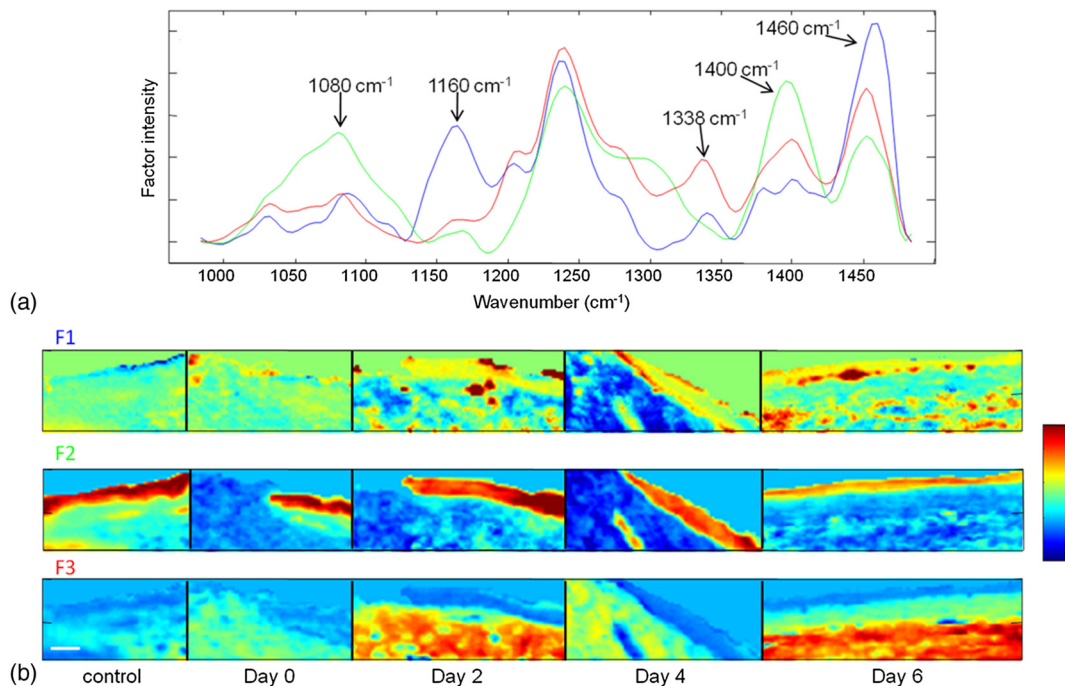


**Fig. 7** IR characterization (factor analysis conducted over the 980 to 1480 cm$^{-1}$ region) of nonwounded control and wounded skin samples at time points zero, two, four, and six days postwounding. (a) Factor loadings of F1 (blue), F2 (green), and F3 (red). (b) Score images of these three factors, showing spatial distribution of different chemical species for the control and day zero, two, four, and six sections as marked. The 100-$\mu$m scale bar applies to all the images.

**Table 1** List of lipid metabolism-related genes regulated two and four days after wounding.

| Fold change Wound/control | | Gene symbol | Unigene component | Function |
|---|---|---|---|---|
| 48 h | 96 h | | | |
| −1.44 | −2.01 | DBT | Dihydrolipoamide branched chain transacylase | Lipid metabolism |
| −2.33 | 1.30 | DLST | Dihydrolipoamide *S*-succinyltransferase | Lipid metabolism |
| 3.28 | 2.80 | FABP4 | Fatty acid binding protein 4, adipocyte | Lipid metabolism |
| 2.27 | 5.06 | FADS1 | Fatty acid desaturase 1 | Lipid metabolism |
| 1.63 | 2.48 | FADS3 | Fatty acid desaturase 3 | Lipid metabolism |
| 1.02 | 2.47 | HELO1 | Homolog of yeast long chain polyunsaturated fatty acid elongation enzyme 2 | Lipid metabolism |
| −2.46 | 4.76 | LOC51601 | Lipoyltransferase | Lipid metabolism |
| −1.10 | −2.22 | PAFAH2 | Platelet-activating factor acetylhydrolase 2 | Lipid metabolism |
| −1.23 | 2.22 | PLSCR1 | Phospholipid scramblase 1 | Lipid metabolism |
| 1.07 | 4.65 | SAA1 | Serum amyloid A1 | Lipid metabolism |
| 2.32 | 1.17 | SCD | Stearoyl-CoA desaturase | Lipid metabolism |
| 1.19 | −2.19 | SDR1 | Short-chain dehydrogenase/reductase 1 | Lipid metabolism |
| 1.56 | 3.91 | EDG2 | Endothelial differentiation, lysophosphatidic acid G-protein-coupled receptor, 2 | Receptor, G-protein-coupled |
| −4.01 | −2.50 | HMGCS1 | 3-Hydroxy-3-methylglutaryl-Coenzyme A synthase 1 | Steroid metabolism |

score images [Fig. 7(b)]. High scores for factor loading 1 (F1) map to the regions previously assigned to disordered lipid [Fig. 4(b), L2] and a relatively higher ester C = O content [Fig. 5(b)]. Correlating the three images, we tentatively assign the 1160 cm$^{-1}$ band to the C-O single bond stretch of the ester group. The fact that the methylene bending mode, ~1460 cm$^{-1}$, is the highest-intensity band in F1 is also consistent with the presence of lipid in these regions. Thus, the proposition that disordered lipids are present in regions below and within the lower areas of the MET is reasonably justified. Score images for the remaining two factor loadings, F2 and F3, display discrete spatial distributions readily assigned to keratin in the epidermis and collagen in the dermis, respectively. In addition, several spectral features observed in the loadings along with factor analysis in the Amide I and II region (data not shown) are consistent with this assignment. For example, the intense band at ~1400 cm$^{-1}$ in F2 arises from the symmetric carboxylate stretch. Keratin has a larger percentage of glu and asp that contain carboxylate side chains than collagen, thus indicating its presence. The loading F3, arising from the collagen-rich dermis, is also confirmed by the presence of the 1338 cm$^{-1}$ peak. This mode has been tentatively assigned as a CH$_2$ wagging mode of the proline ring.[23]

### 3.2 *Gene Expression Analyses Reveal Deregulation of Genes Involved in Lipid Metabolism*

Microarray analyses were utilized to study gene expression in *ex vivo* wounded skin specimens two and four days postwounding compared to healthy control skin (Table 1). Changes were detected in genes involved in lipid metabolism. Fatty acid desaturases 1 and 3 (FADS1 and FADS3), enzymes that regulate unsaturation of fatty acids through the introduction of double bonds between defined carbons of the acyl chain, were induced over the four-day time period. In contrast, after an initial induction of stearoyl-CoA desaturase (SCD) at two days postwounding, expression decreased by day four. The principal product of SCD is oleic acid formed by desaturation of stearic acid. Furthermore, suppression of 3-hydroxy-3-methylglutaryl-Coenzyme A synthase 1 (HMGCS1) was found at both time points tested. This enzyme catalyzes the reaction in which Acetyl-CoA condenses with acetoacetyl-CoA to form 3-hydroxy-3-methylglutaryl-CoA (HMG-CoA), an intermediate in cholesterol synthesis, indicating deregulation of, and in this case, a decrease in cholesterol synthesis.

## 4  Discussion

In this study we observed a disordered lipid phase in the wound area and characterized its spatial and temporal evolution as healing progressed through six days in *ex vivo* skin wounds. Lipid physical state in the vicinity of the MET has neither been observed experimentally nor discussed significantly in the literature to date. However, several biochemical lines of published work provide a useful frame of reference for interpretation of the current results.

The disordered lipid phase is characterized by a factor loading whose spatial distribution of high scores tracks the areas near and within the MET reasonably well in the two to six day stages of healing. The lipid chains are conformationally more disordered than those in the SC and in the control section VE (Fig. 4) as characterized by symmetric CH$_2$ stretching

frequencies at ~2854.5 cm$^{-1}$ and asymmetric CH$_2$ stretching frequencies at ~2925 cm$^{-1}$. This conclusion is reached because of the unique ability of IR to directly image lipid conformational order.

Three IR spectral regions provide evidence for the presence and involvement of disordered, ester-containing lipids during the wound healing (Figs. 4, 5, and 7). Although factor analysis provides an important qualitative evaluation of spectral differences related to composition and molecular structure, a semiquantitative assessment of the evolution of particular features is better accomplished by univariate techniques (Figs. 5 and 6). Thus, the integrated area of the CH$_2$ symmetric stretching mode in Figs. 5(a) and 6(b) provides direct evidence for a progressive increase in the amount of lipid within and in the vicinity of the MET as healing progresses compared to the VE in the control section. In these figures, the relatively high amount of lipid in the SC is also evident, as anticipated, and will not be considered further. Comparing Fig. 5(a) to the factor score images derived from the CH stretching region in Fig. 4, it is clear that the regions within and in the vicinity of the MET with a higher lipid content [Fig. 5(a)] more closely coincide with the factor score images for the "disordered," L2, lipid constituent and not L1, the ordered lipid constituent [Fig. 4(b)].

Gene array analysis provides some evidence for an increase in the unsaturated lipid population through the induction of the fatty acid desaturases, FADS1 and FADS3 (Table 1). Unsaturation in lipid acyl chains generally increases conformational disorder. An obvious issue to consider is the relationship of this disordered lipid to keratinocyte behavior during the re-epithelization phase of wound healing.

One possible role for the increase in disordered lipid population related to wound healing may involve the EGFR, known to activate keratinocytes upon ligand binding.[24] Elevation of EGFR regulates a wide range of cellular processes that are important during wound healing, including cell adhesion, expression of matrix proteinases, and keratinocyte proliferation and migration.[25,26] Of interest in the current work is the possible role of the physical state of lipid in the receptor environment on the control of EGFR function. Several studies addressing this issue have suggested receptor localization in lipid rafts,[17–20,27] cholesterol enriched domains involved in signal transduction. Pike et al.[17] reported that the EGFR-enriched lipid rafts are augmented in lipid classes that differ from those identified by the classical Triton X-100 extraction procedure that first defined lipid rafts. They suggest that unlike "traditional" raft composition, EGFR-containing rafts have a lower degree of chain saturation.[17] This suggests that the EGFR-enriched rafts are likely to be conformationally less ordered than "traditional" rafts, and are certainly much less ordered than SC lipids. Thus, it is tempting to speculate that the disordered lipid population observed in the current experiments may participate in EGFR activation and internalization. To discern whether the increase in the disordered lipids we observe in the MET is involved in the EGFR raft environment and/or internalization will require additional study.

The observed increase in the relative amount of disordered lipids within and in the vicinity of the MET could certainly be involved in additional functions related to wound healing. Some wound healing events directly involve lipids, although the conformational state of the lipids has not been reported. These may include the active involvement of phosphatidic acid,[28] phosphoinositides, or diacylglycerol[25,29] in cell signaling or an increase in triglycerides as a source of energy for cell proliferation and

migration as suggested by Kozel'tsev et al.[15] Other work, including the microarray analysis herein, suggests the indirect involvement of lipids in wound healing. The induction of the endothelial differentiation, lysophosphatidic acid G-protein-couple receptor 2 (EDG2) gene (Table 1), known to mediate proliferation among other functions, implies that the presence of lysophosphatidic acid is increased. Finally, an increase in a lipid population with relatively high acyl chain conformational disorder would tend to increase lipid diffusion rates, thus providing a more fluid environment for the migration of keratinocytes.

In summary, IR imaging data detects the presence and spatial distribution of a disordered lipid phase within and in the vicinity of the MET as healing progresses (days two to six) in the current *ex vivo* wound healing sections. Several possibilities are noted above for the biological relevance of these observations. Further mechanistic insight may be gained from molecular biology approaches such as immunofluorescent staining in an attempt to specify, for example, lipid involvement with EGFR activation. The current work likely provides some hypotheses to be tested in these further studies.

## References

1. A. J. Singer and R. A. F. Clark, "Cutaneous wound healing," *N. Engl. J. Med.* **341**(10), 738–746 (1999).
2. K. L. A. Chan et al., "A coordinated approach to cutaneous wound healing: vibrational microscopy and molecular biology," *J. Cell. Mol. Med.* **12**(5B), 2145–2154 (2008).
3. G. K. Patel et al., "Numerous keratinocyte subtypes involved in wound re-epithelialization," *J. Invest. Dermatol.* **126**(2), 497–502 (2006).
4. M. L. Usui et al., "Morphological evidence for the role of suprabasal keratinocytes in wound reepithelialization," *Wound Repair Regen.* **13**(5), 468–479 (2005).
5. G. Zhang et al., "Vibrational microscopy and imaging of skin: from single cells to intact tissue," *Anal. Bioanal. Chem.* **387**(5), 1591–1599 (2007).
6. R. Mendelsohn et al., "Infrared microspectroscopic imaging maps the spatial distribution of exogenous molecules in skin," *J. Biomed. Opt.* **8**(2), 185–190 (2003).
7. E. Gazi et al., "Direct evidence of lipid translocation between adipocytes and prostate cancer cells with imaging FTIR microspectroscopy," *J. Lipid Res.* **48**(8), 1846–1856 (2007).
8. G. Zhang et al., "Imaging the prodrug-to-drug transformation of a 5-Fluorouracil derivative in skin by confocal Raman microscopy," *J. Invest. Dermatol.* **127**(5), 1205–1209 (2007).
9. G. Zhang et al., "Vibrational microspectroscopy and imaging of molecular composition and structure during human corneocyte maturation," *J. Invest. Dermatol.* **126**(5), 1088–1094 (2006).
10. D. J. Moore, M. E. Rerek, and R. Mendelsohn, "Lipid domains and orthorhombic phases in model stratum corneum: evidence from Fourier transform infrared spectroscopy studies," *Biochem. Biophys. Res. Commun.* **231**(3), 797–801 (1997).
11. R. D. Pensack et al., "Infrared kinetic/structural studies of barrier reformation in intact stratum corneum following thermal perturbation," *Appl. Spectrosc.* **60**(12), 1399–1404 (2006).
12. M. Boncheva, F. Damien, and V. Normand, "Molecular organization of the lipid matrix in intact stratum corneum using ATR-FTIR spectroscopy," *Biochim. Biophys. Acta* **1778**(5), 1344–1355 (2008).
13. G. S. Gooris and J. A. Bouwstra, "Infrared spectroscopic study of stratum corneum model membranes prepared from human ceramides, cholesterol, and fatty acids," *Biophys. J.* **92**(8), 2785–2795 (2007).
14. R. Mendelsohn and H. H. Mantsch, "Fourier transform infrared studies of lipid-protein interaction," in *Progress in Protein-Lipid Interaction*, A. Watts and J. J. H. M. de Pont, eds., Elsevier, Amsterdam, Vol. 2, pp. 103–146 (1986).

15. V. L. Kozel'tsev et al., "Changes in wound field lipids in rat skin," *Bull. Exp. Biol. Med.* **142**(4), 493–494 (2006).
16. J. Vicanova et al., "Stratum corneum lipid composition and structure in cultured skin substitutes is restored to normal after grafting onto athymic mice," *J. Invest. Dermatol. Symp. Proc.* **3**(2), 114–120 (1998).
17. L. J. Pike, X. Han, and R. W. Gross, "Epidermal growth factor receptors are localized to lipid rafts that contain a balance of inner and outer leaflet lipids," *J. Biol. Chem.* **280**(29), 26796–26804 (2005).
18. T. Ringerike et al., "Cholesterol is important in control of EGF receptor kinase activity but EGF receptors are not concentrated in caveolae," *J. Cell Sci.* **115**(6), 1331–1340 (2001).
19. S. Lambert et al., "Internalization of EGF receptor following lipid rafts disruption in keratinolcytes is delayed and dependent on p38 MAPK activation," *J. Cell. Physiol.* **217**(3), 834–845 (2008).
20. C. Mathay et al., "Heparin-binding EGF-like growth factor is induced by disruption of lipid rafts and oxidative stress in keratinocytes and participates in the epidermal response to cutaneous wounds," *J. Invest. Dermatol.* **128**(3), 717–727 (2008).
21. M. Tomic-Canic et al., "Streptolysin O enhances keratinocyte migration and proliferation and promotes skin organ culture wound healing *in vitro*," *Wound Repair Regen.* **15**(1), 71–79 (2007).
22. P. A. Coulombe, "Wound epithelialization: accelerating the pace of discovery," *J. Invest. Dermatol.* **121**(2), 219–230 (2003).
23. M. Jackson et al., "Beware of connective tissue proteins: assignment and implications of collagen absorption in infrared spectra of human tissues," *Biochim. Biophys. Acta* **1270**(1), 1–6 (1995).
24. C.-K. Jiang et al., "Epidermal growth factor and transforming growth factor a specifically induce the activation- and hyperproliferation-associated keratine 6 and 16," *Proc. Natl. Acad. Sci. USA* **90**(14), 6786–6790 (1993).
25. L. G. Hudson and L. J. McCawley, "Contributions of the epidermal growth factor receptor to keratinocyte motility," *Microsc. Res. Tech.* **43**(5), 444–455 (1998).
26. S. K. Repertinger et al., "EGFR enhances early healing after cutaneous incisional wounding," *J. Invest. Dermatol.* **123**(5), 982–989 (2004).
27. A. Balbis and B. I. Posner, "Compartmentalization of EGFR in cellular membranes: role of membrane rafts," *J. Cell. Biochem.* **109**(6), 1103–1108 (2010).
28. A. R. Mazie et al., "Epithelial cell motility is triggered by activation of the EGR receptor through phosphatidic acid signaling," *J. Cell Sci.* **119**(8), 1645–1654 (2006).
29. S. Lambert, R. Gniadecka, and Y. Poumay, "Cholesterol and lipid rafts as regulators of signaling through the EGF receptor in keratinocytes," *Open Dermatol. J.* **3**(2), 151–158 (2009).